Annexin A2 supports pulmonary microvascular integrity by linking vascular endothelial cadherin and protein tyrosine phosphatases

Min Luo,[1] Elle C. Flood,[2] Dena Almeida,[1] LunBiao Yan,[2] David A. Berlin,[3] Paul M. Heerdt,[4] and Katherine A. Hajjar[1,2,3]

[1]Department of Pediatrics, [2]Department of Cell and Developmental Biology, [3]Department of Medicine, and [4]Department of Anesthesiology, Weill Cornell Medical College, New York, NY

Relative or absolute hypoxia activates signaling pathways that alter gene expression and stabilize the pulmonary microvasculature. Alveolar hypoxia occurs in disorders ranging from altitude sickness to airway obstruction, apnea, and atelectasis. Here, we report that the phospholipid-binding protein, annexin A2 (ANXA2) functions to maintain vascular integrity in the face of alveolar hypoxia. We demonstrate that microvascular endothelial cells (ECs) from *Anxa2*$^{-/-}$ mice display reduced barrier function and excessive Src-related tyrosine phosphorylation of the adherens junction protein vascular endothelial cadherin (VEC). Moreover, unlike *Anxa2*$^{+/+}$ controls, *Anxa2*$^{-/-}$ mice develop pulmonary edema and neutrophil infiltration in the lung parenchyma in response to subacute alveolar hypoxia. Mice deficient in the ANXA2-binding partner, S100A10, failed to demonstrate hypoxia-induced pulmonary edema under the same conditions. Further analyses reveal that ANXA2 forms a complex with VEC and its phosphatases, EC-specific protein tyrosine phosphatase (VE-PTP) and Src homology phosphatase 2 (SHP2), both of which are implicated in vascular integrity. In the absence of ANXA2, VEC is hyperphosphorylated at tyrosine 731 in response to vascular endothelial growth factor, which likely contributes to hypoxia-induced extravasation of fluid and leukocytes. We conclude that ANXA2 contributes to pulmonary microvascular integrity by enabling VEC-related phosphatase activity, thereby preventing vascular leak during alveolar hypoxia.

The Journal of Experimental Medicine

INTRODUCTION

The pulmonary capillary endothelium consists of a continuous layer of nonfenestrated cells linked by comingled elements of adherens, tight, and gap junction proteins and forming a 0.1-µm vascular–alveolar interface that is highly adapted for efficient gas exchange (Townsley, 2012). Phosphorylation of vascular endothelial cadherin (VEC) by Src kinase, and its dephosphorylation by specific phosphatases, regulates homotypic VEC–VEC connections, thereby controlling extravasation of fluid and leukocytes. Under hypoxia, expression of vascular endothelial growth factor (VEGF) increases upon stabilization of hypoxia-inducible factors (Manalo et al., 2005), and may trigger Src-mediated tyrosine phosphorylation of VEC at tyrosines 685 or 731 (pY731-VEC), in association with disruption of VEC–VEC adhesive interactions (Dejana and Vestweber, 2013). VEGF, also known as vascular permeability factor, is highly expressed in the lung, and its overproduction results in pulmonary edema (Kaner et al., 2000). Dephosphorylation of VEC is thought to depend upon several phosphatases, including vascular endothelial protein tyrosine phosphatase (VE-PTP), the mouse homologue of human PTP-β (Nawroth et al., 2002; Küppers et al., 2014), and Src homology phosphatase 2 (SHP2; Grinnell et al., 2010; Küppers et al., 2014). Annexin A2 (ANXA2) is a hypoxia-regulated, phospholipid-binding protein that is among the 3% most abundantly expressed plasma membrane proteins in lung endothelium (Durr et al., 2004; Huang et al., 2011; Luo and Hajjar, 2013). Its depletion in cultured HUVECs leads to increased pY-VEC and loss of barrier function (Heyraud et al., 2008; Su et al., 2010). Here, we report that ANXA2 associates with VEC, VE-PTP, and SHP2 in the lung vasculature, thereby supporting efficient VEC phosphatase activity and maintaining pulmonary vascular integrity under hypoxia.

RESULTS AND DISCUSSION

As previously reported (Heyraud et al., 2008; Su et al., 2010), we noted that the rate of translocation of high-molecular-weight

Correspondence to Katherine A. Hajjar: khajjar@med.cornell.edu

L. Yan's present address is Dept. of Medicine, Weill Cornell Medical College, New York, NY.

P.M. Heerdt's present address is Dept. of Anesthesiology, Yale University School of Medicine, New Haven, CT.

Abbreviations used: BAL, bronchial alveolar lavage; CMEC, cardiac microvascular EC; EB, Evans blue dye; EC, endothelial cell; IEM, immunoelectron microscopy; LMEC, lung microvascular EC; PTP, protein tyrosine phosphatase; TEER, transendothelial electrical resistance; VEC, vascular endothelial cadherin; VEGF, vascular endothelial growth factor.

© 2017 Luo et al. This article is distributed under the terms of an Attribution–Noncommercial–Share Alike–No Mirror Sites license for the first six months after the publication date (see http://www.rupress.org/terms/). After six months it is available under a Creative Commons License (Attribution–Noncommercial–Share Alike 4.0 International license, as described at https://creativecommons.org/licenses/by-nc-sa/4.0/).

The Rockefeller University Press
J. Exp. Med. 2017 Vol. 214 No. 9 2535–2545
https://doi.org/10.1084/jem.20160652

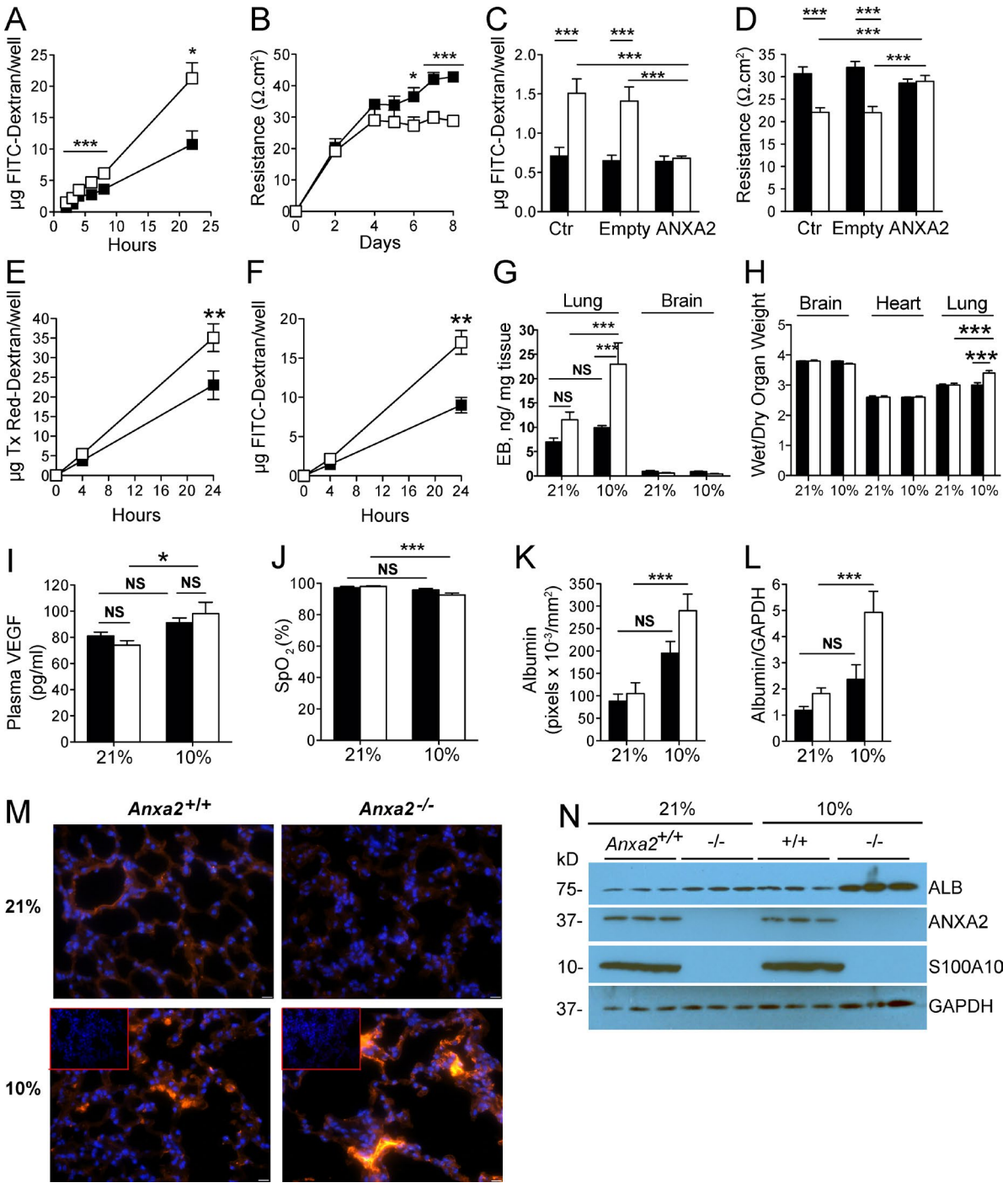

Figure 1. **ANXA2 supports EC barrier function in vitro and vascular integrity in the hypoxic lung.** (A) Permeability of confluent *Anxa2*$^{+/+}$ and *Anxa2*$^{-/-}$ CMEC monolayers to 2,000-kD FITC–dextran assessed over 24 h (n = 3 replicates, Student's t test). (B) TEER measured across confluent CMEC monolayers on days 2–8 (n = 3–9, Student's t test). (C and D) CMEC monolayers were transduced with empty or ANX2-encoding adenovirus, and permeability to FITC–dextran (n = 6 replicates, ANOVA) was assessed over a 2-h period and TEER (n = 10 replicates, ANOVA) over 60 h. (E and F) Permeability of confluent *Anxa2*$^{+/+}$ and *Anxa2*$^{-/-}$ LMEC monolayers to 40-kD Texas red–dextran (E) or 500-kD FITC–dextran (F) over 24 h (n = 3 replicates, Student's t test). (G) EB was extracted from lung and brain from highly perfused *Anxa2*$^{+/+}$ and *Anxa2*$^{-/-}$ normoxic or posthypoxic mice (n = 5–6 replicates, ANOVA). (H) Corresponding wet/dry weight organ ratios (n = 6 replicates, ANOVA), plasma VEGF levels (I; n = 6 replicates, ANOVA), and hemoglobin saturation (J; n = 7–16; replicates, ANOVA) were assayed. (K) Image analysis of sections (M) stained for extravascular albumin in five random images from each of three mice per group. Insets show no primary antibody control. Bars, 20 µm. (L) Densitometric analysis of immunoblots

FITC–dextran across confluent ANXA2-deficient cardiac microvascular endothelial cell (EC [CMEC]) monolayers was twice that observed for wild type CMECs (Fig. 1 A). Similarly, transendothelial electrical resistance (TEER) values for *Anxa2*$^{+/+}$ CMEC monolayers increased steadily over the first week in culture, whereas TEER for *Anxa2*$^{-/-}$ CMECs plateaued at a lower level (Fig. 1 B). On day 8 postconfluency, TEER values were 50% higher in *Anxa2*$^{+/+}$ CMECs than in *Anxa2*$^{-/-}$ CMECs. Infection of *Anxa2*$^{-/-}$ CMEC monolayers with an ANXA2-encoding virus restored both FITC–dextran translocation and TEER to levels observed in noninfected *Anxa2*$^{+/+}$ cells or *Anxa2*$^{+/+}$ cells infected with either empty or ANXA2-encoding viruses (Fig. 1, C and D). Loss of ANXA2 in lung microvascular ECs (LMECs) led to a relative loss of barrier function that was similar to that seen in CMECs (Fig. 1, E and F). Therefore, we used CMECs in subsequent experiments because of their greater purity and improved yield.

We next exposed *Anxa2*$^{-/-}$ and *Anxa2*$^{+/+}$ mice to either 21% or 10% ambient O_2 for 48 h. In vivo assessment of vascular barrier function using Evans blue dye (EB) revealed minimal extravasation of EB into the brain parenchyma for both genotypes regardless of ambient O_2 but a twofold increase in EB leakage into the lung parenchyma in *Anxa2*$^{-/-}$ mice compared with *Anxa2*$^{+/+}$ mice after treatment with 10% O_2 (Fig. 1 G). Similarly, organ wet/dry weight ratios increased only in the posthypoxic *Anxa2*$^{-/-}$ lung, but not in heart or brain (Fig. 1 H). Although plasma VEGF levels did not differ significantly between genotypes (Fig. 1 I), pulse oximetry revealed significantly reduced hemoglobin saturation (Fig. 1 J), and immunohistologic and immunoblot analyses showed significantly increased extravascular albumin in the lung in *Anxa2*$^{-/-}$ mice immediately upon release from hypoxia (Fig. 1, K–N), suggesting vascular compromise in vivo.

Hematoxylin and eosin–stained sections of fixed lung showed no difference in septal thickness or inflammatory cell number between the two genotypes at baseline (Fig. 2, A and B). After hypoxia, however, scoring based on a standard lung injury paradigm (Aeffner et al., 2015) revealed a doubling in neutrophil infiltration and quadrupling of septal thickness in *Anxa2*$^{-/-}$ lungs (Fig. 2, A and C). These results were confirmed by immunoblot analysis of lung extracts for Ly6G and F4/80 neutrophil and macrophage markers, respectively (Fig. 2, D and E), and suggested that hypoxia-induced vascular leak in the *Anxa2*$^{-/-}$ mouse was associated with extravasation of neutrophils into the lung parenchyma after 2 d.

Because ANXA2 may heterotetramerize with S100A10 in its membrane-associated functions (Luo and Hajjar, 2013), we tested the pulmonary response of *S100a10*$^{-/-}$ mice to hypoxia (Fig. 3). Lung tissue from *S100a10*$^{-/-}$ mice, generated via homologous recombination (Fig. 3, A–C), showed slightly decreased ANXA2 expression, whereas S100A10 protein was almost undetectable in the *Anxa2*$^{-/-}$ lung (Fig. 3 D), reflecting our previous finding that ANXA2 stabilizes S100A10 in ECs by masking a polyubiquitination site that directs S100A10 to the proteasome for degradation. Posthypoxic *S100a10*$^{-/-}$ mice failed to show either increased EB extravasation in the lung (Fig. 3 E) or reduced hemoglobin saturation (Fig. 3 F). Bronchial alveolar lavage (BAL) fluid albumin increased fourfold in posthypoxic *Anxa2*$^{-/-}$, but not *S100a10*$^{-/-}$, mice, which mimicked the wild-type (Fig. 3 G). These data indicate that the ability of ANXA2 to promote pulmonary vascular integrity does not require expression of S100A10.

We next examined the susceptibility of VEC within *Anxa2*$^{-/-}$ and *Anxa2*$^{+/+}$ CMECs to Src-mediated phosphorylation. Pretreatment of CMECs with the Src inhibitor PP2 specifically reduced levels of VEGF-induced pY731-VEC to baseline in both genotypes (Fig. 4 A). PP2 also blocked VEGF-induced permeability to FITC–dextran (Fig. 4 B) and diminished loss of TEER (Fig. 4 C), indicating equal susceptibility of Y731-VEC to Src phosphorylation between the two genotypes.

To identify the sites of VEC tyrosine phosphorylation affected by ANXA2, we used two highly specific monoclonal antibodies directed against pY731 and pY685 (Wessel et al., 2014). In both *Anxa2*$^{-/-}$ and *Anxa2*$^{+/+}$ CMECs, Y731-VEC showed low-level phosphorylation at baseline; upon exposure to VEGF, pY731 increased three- to fivefold in *Anxa2*$^{-/-}$, but not *Anxa2*$^{+/+}$, CMECs (Fig. 4, D and E). Using another highly specific antibody (Wessel et al., 2014), as well as a commercial IgG, we found no significant increase in pY685-VEC under the same conditions (Fig. 4 F). Interestingly, pY685-VEC is known to be dephosphorylated by VE-PTP, whereas pY731-VEC is not (Wessel et al., 2014). Therefore, we examined two other VE-PTP targets, Tie2 (pY992; Fig. 4 G) and VEGFR2 (pY1175; not depicted) and found that neither protein was hyperphosphorylated in VEGF-stimulated *Anxa2*$^{-/-}$ cells. This result suggested that VE-PTP activity was not altered in the absence of ANXA2 and raised the possibility that another phosphatase might regulate pY731-VEC. Indeed, it has been reported that catalytically inactive VE-PTP still supports vascular integrity, leading to the hypothesis that VE-PTP might either recruit or activate another phosphatase (Nawroth et al., 2002). Together, these data suggested that a non–VE-PTP phosphatase might regulate vascular integrity in an ANXA2-dependent manner under VEGF stimulation.

Confocal microscopy of lung sections demonstrated regions of close proximity of VEC and ANXA2 near the luminal surface of microvessels (Fig. 5 A, left and right).

of whole-lung protein (N) from highly perfused lung tissue (n = 3 mice per group, ANOVA). Data in A, B, and C–N are representative of nine, six, and three experiments, respectively. Black and white squares or bars indicate *Anxa2*$^{+/+}$ and *Anxa2*$^{-/-}$ cells or mice, respectively. Data are expressed as mean ± SEM. *, P < 0.05; **, P < 0.01; ***, P < 0.001.

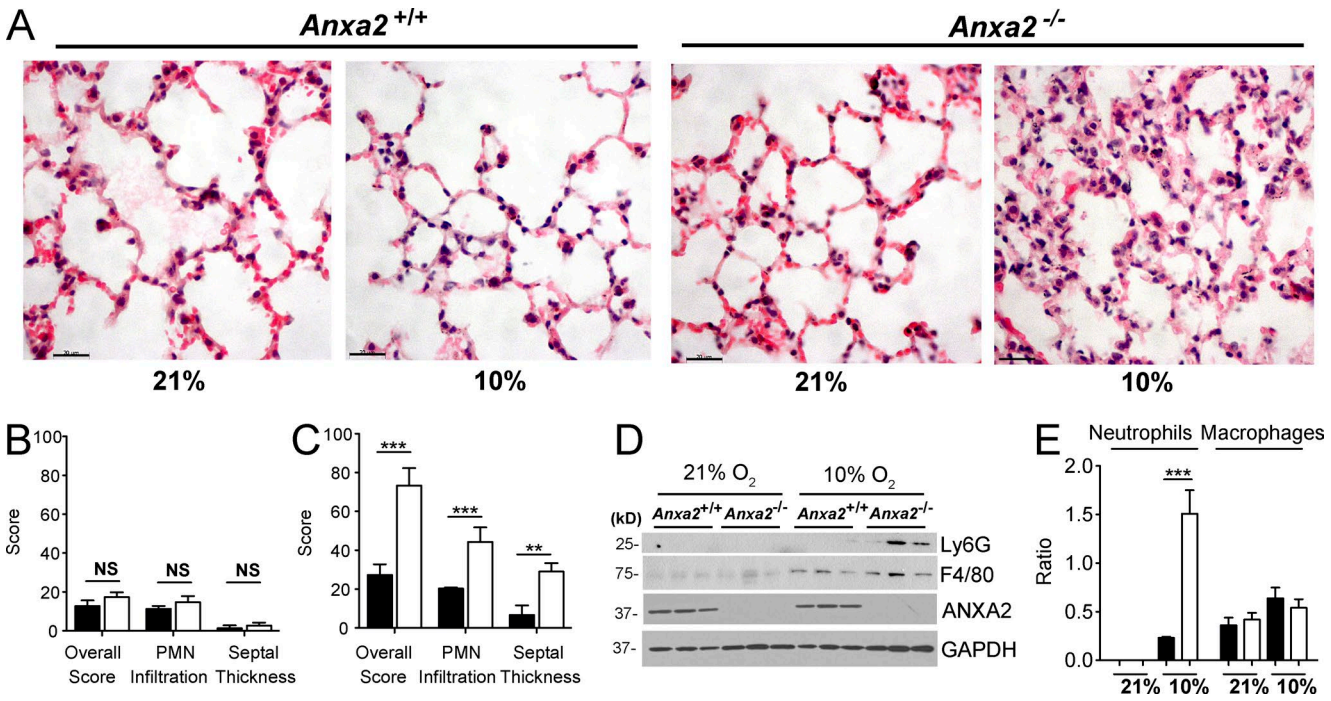

Figure 2. **Leukocyte extravasation in the posthypoxic *Anxa2*$^{-/-}$ lung.** (A) Representative images of hematoxylin and eosin–stained sections from *Anxa2*$^{+/+}$ and *Anxa2*$^{-/-}$ normoxic or posthypoxic lungs. Bars, 20 µm. (B and C) Quantification of inflammatory cell infiltration and septal thickness in 20 random sections from each of three highly perfused lungs from *Anxa2*$^{+/+}$ or *Anxa2*$^{-/-}$ normoxic (B) or posthypoxic (C) mice (ANOVA). (D) Immunoblot of lung homogenates from three separate animals for neutrophil (Ly6G) and macrophage (F4/80) markers. Results in A–E are representative of three separate experiments. (E) Quantification of immunoblotted Ly6G/GAPDH and F4/80/GAPDH ratios from (D; n = 3 mice per group, ANOVA). Black and white bars indicate *Anxa2*$^{+/+}$ and *Anxa2*$^{-/-}$ mice, respectively. Data are expressed as mean ± SEM. **, P < 0.01; ***, P < 0.001.

Immunoelectron microscopy (IEM) similarly, identified co-clusters of anti–ANXA2- and anti–VEC-conjugated gold particles within ECs (Fig. 5 B, left and right). In pull-down experiments, anti–VEC antibodies precipitated ANXA2, but not ANXA4 (Fig. 5 C). Further confocal microscopy unveiled focal association of ANXA2 and VE-PTP within microvessels (Fig. 5 D, left and right), and IEM demonstrated a close association between ANXA2 and VE-PTP (Fig. 5 E, left and right), as well as VEC and VE-PTP (Fig. 5 F, left and right). Together, these data indicated that ANXA2 interacts with both VEC and VE-PTP.

To determine whether VEGF-induced permeability in the *Anxa2*$^{-/-}$ microvasculature reflects impaired dephosphorylation of pY-VEC, we used the Miles assay. After intradermal injection of VEGF, we found a nearly twofold increase in extravasation of EB in *Anxa2*$^{-/-}$ versus *Anxa2*$^{+/+}$ mice (Fig. 5 G). Pretreatment with a fibrinogen-depleting agent (Ancrod) failed to increase cutaneous capillary leak, indicating that increased vascular permeability in *Anxa2*$^{-/-}$ mice is independent of fibrin deposition (not depicted). Treatment of *Anxa2*$^{+/+}$ mice with the general phosphatase inhibitor sodium orthovanadate increased VEGF-induced EB extravasation to the level seen in the untreated *Anxa2*$^{-/-}$ mouse, whereas a seryl-threonyl-phosphatase inhibitor (sodium fluoride) had no effect (Fig. 5 H). Therefore, acutely increased VEGF-induced permeability of *Anxa2*$^{-/-}$ vasculature reflected loss of tyrosine phosphatase activity.

The phosphatase SHP2 has been implicated in the regulation of edemogenic VEC phosphorylation in the lung (Grinnell et al., 2010), has been demonstrated to interact with ANXA2 at EC junctions (Burkart et al., 2003), and has been shown to regulate pY731-VEC dephosphorylation (Wessel et al., 2014). In pull-down experiments, anti–VEC IgG coprecipitated VE-PTP, ANXA2, and SHP2 from *Anxa2*$^{+/+}$ lung extracts; however, pull-down of both VE-PTP and SHP2 was markedly reduced in *Anxa2*$^{-/-}$ lung extracts (Fig. 5, I and J). Similarly, precipitation by anti–VE-PTP of SHP2 along with VEC was reduced by ∼40% and 80%, respectively, in *Anxa2*$^{-/-}$ lung extracts (Fig. 5, K and L). These data suggested that VEC, VE-PTP, and SHP2 form an ANXA2-dependent complex that may enable SHP2-mediated dephosphorylation of Y731-VEC.

These data provide physical and biochemical evidence that ANXA2 supports microvascular integrity in the hypoxic lung. We show that ANXA2 contributes to the dephosphorylation of Y731-VEC, most likely by supporting the assembly of a complex that includes ANXA2, VEC, VE-PTP, and SHP2. SHP2 has been previously shown to target pY731-VEC in ECs (Wessel et al., 2014), and we find elevated levels of VEGF-induced Y731-VEC in *Anxa2*$^{-/-}$ CMECs. The asso-

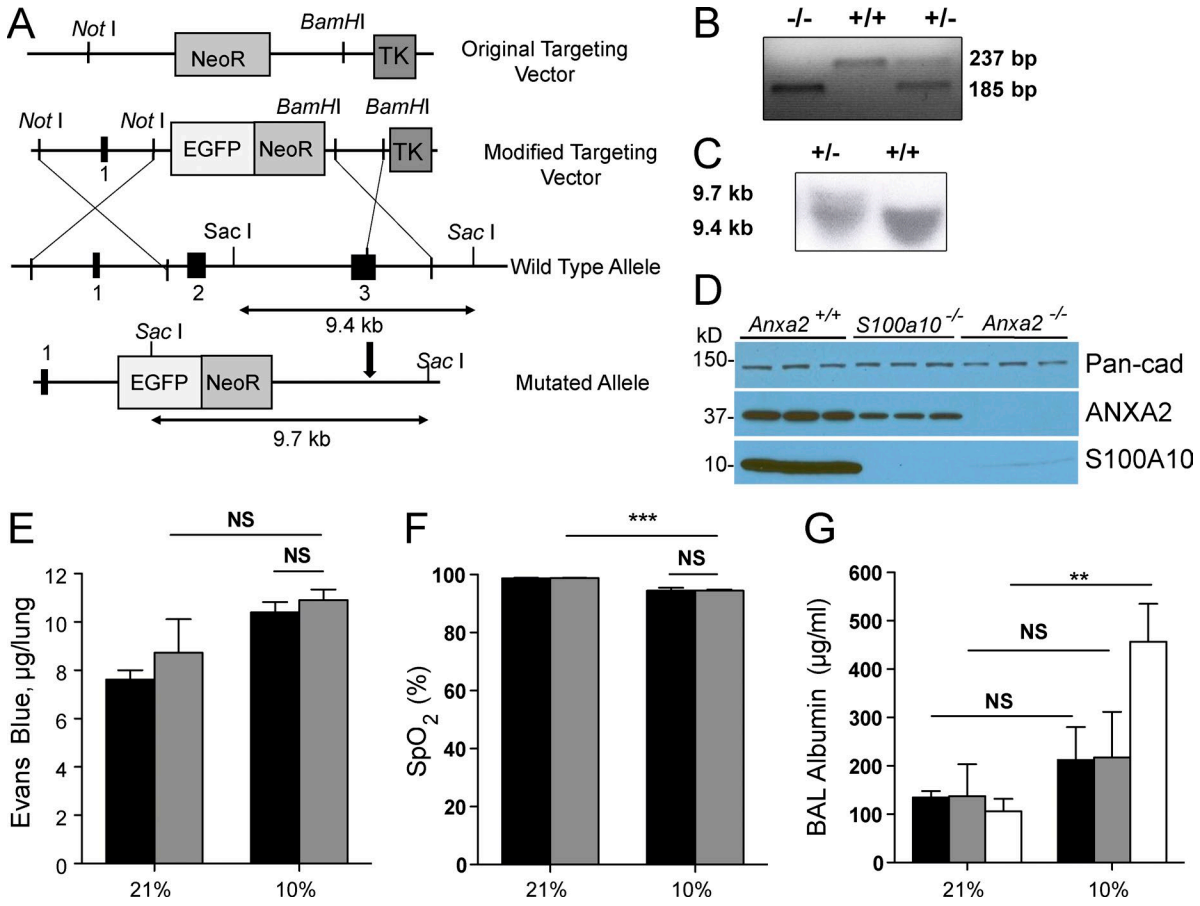

Figure 3. **Pulmonary vascular integrity in the *S100a10*$^{-/-}$ mouse.** (A) Genomic organization of wild type and targeted alleles after homologous recombination. *SacI* fragments for wild-type and mutant alleles are indicated by double-headed arrows. Numerals 1–3 refer to exons. The vertical arrow indicates the binding site for the Southern blot probe. (B and C) PCR and Southern blot analysis of tail tip DNA from founder mice (*S100a10*$^{+/-}$ or *S100a10*$^{+/+}$). In C, fragments correspond to wild-type (9.4 kb) and mutant (9.7 kb) alleles. (D) Immunoblot of pan-cadherin (loading control), ANXA2, and S100A10 in lung tissue extracts from wild-type, *S100a10*$^{-/-}$, and *Anxa2*$^{-/-}$, mice. (E) EB extracted from whole lung tissue from *S100a10*$^{+/+}$ and *S100a10*$^{-/-}$ mice treated with FiO_2 0.21 or 0.10 (48 h, $n = 5$ animals per group, ANOVA). (F) Pulse oximetry estimation of hemoglobin saturation for *S100a10*$^{+/+}$ and *S100a10*$^{-/-}$ mice treated as in E ($n = 8$–9 per group, ANOVA). (G) ELISA of albumin in BAL fluid from wild-type, *S100a10*$^{-/-}$, and *Anxa2*$^{-/-}$ mice maintained at FiO_2 0.21 or 0.10 for 48 h ($n = 4$–7 mice per group, ANOVA). All data are representative of three to six separate experiments. Wild-type, *S100a10*$^{-/-}$, and *Anxa2*$^{-/-}$ mice are indicated by black, gray, and white bars, respectively. Data are expressed as mean ± SEM. **, $P < 0.01$; ***, $P < 0.001$.

ciation of hyperphosphorylation of Y731 with both vascular leak and extravasation of leukocytes appears to differ from the elegant findings of Wessel et al. (2014), whereby phosphorylation of Y731 was linked to extravasation of leukocytes, whereas phosphorylation of Y685 correlated with leakage of fluid. These differences warrant further investigation in view of studies showing that site-specific phosphorylation may depend upon the pathophysiologic setting and vascular bed of interest (Orsenigo et al., 2012; Wessel et al., 2014).

Down-regulation of VE-PTP or its dissociation from VEC is followed by leukocyte transmigration across inflamed endothelium (Nottebaum et al., 2008; Vockel and Vestweber, 2013), providing a possible explanation for our observation of increased numbers of neutrophils in the posthypoxic *Anxa2*$^{-/-}$ lung parenchyma. Maldistribution of intercellular adhesion molecule 1 has been found to occur on the surface of TNFα-treated, ANXA2-depleted ECs and can contribute to augmented neutrophil transmigration (Heemskerk et al., 2016). This phenomenon could be relevant in the hypoxic *Anxa2*$^{-/-}$ mouse, even though baseline expression of cell surface intercellular adhesion molecule and pY14-caveolin did not differ between the two genotypes. In conclusion, ANXA2 appears to regulate extravasation of both fluid and leukocytes in the hypoxic lung, suggesting that a more complete understanding of these mechanisms could enable more effective therapeutic interventions for the pulmonary consequences of hypoxia.

MATERIALS AND METHODS

Microvascular ECs and barrier function

CMECs were isolated from hearts of P2 pups (Ling et al., 2004) and propagated in DMEM containing nutrient mix-

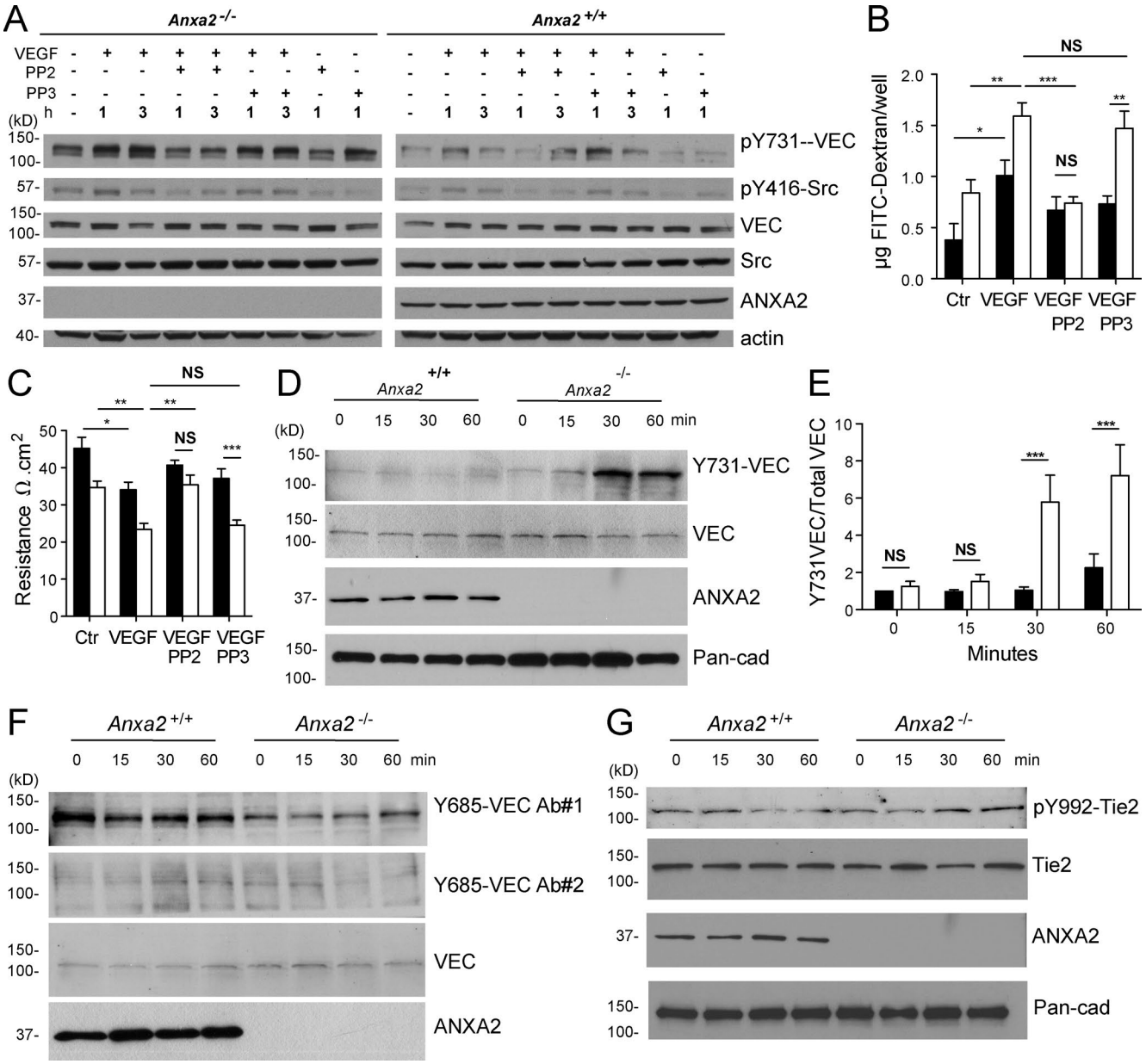

Figure 4. **Effect of ANXA2 on VEC phosphorylation.** (A) After stimulation with rVEGF (0–3 h) in the presence or absence of the Src inhibitor PP2, or control PP3, extracts of confluent *Anxa2*$^{+/+}$ and *Anxa2*$^{-/-}$ CMECs were immunoblotted with anti–pY731-VEC, -pY416-Src-, -VEC, -Src, -ANXA2, and -actin. (B and C) Permeability to FITC–dextran and TEER of CMECs treated with or without recombinant VEGF in the presence or absence of PP2 or PP3 (n = 6 samples per group, ANOVA). (D) Lysates from VEGF-treated *Anxa2*$^{+/+}$ and *Anxa2*$^{-/-}$ CMECs were immunoblotted with anti–pY731-VEC (pY731-73.1, courtesy of D. Vestweber; Wessel et al., 2014), -VEC, -ANXA2, and –pan-cadherin (Pan-cad). (E) Quantification of blots described in D (combined data from 11 experiments, ANOVA). (F) Lysates were blotted with two anti–pY685-VEC antibodies (Ab#1: ab119785; Abcam; and Ab#2: PhoCad3.3, courtesy of D. Vestweber; Wessel et al., 2014), as well as anti-VEC and anti-ANXA2. (G) Lysates were blotted with anti-pY992-Tie2, -Tie2, -ANXA2, and –pan-cadherin. Data in A–C, F, and G are representative of three experiments, and data in D and E are representative of 11 experiments. Black and white bars indicate *Anxa2*$^{+/+}$ and *Anxa2*$^{-/-}$, respectively. Data are expressed as mean ± SEM. *, P < 0.05; **, P < 0.01; ***, P < 0.001.

ture F12 (Gibco), 5% fetal bovine serum (Gibco), 20 µg/ml EC growth supplement (Sigma-Aldrich), 1× EC growth factor (Sigma-Aldrich), 1× insulin–transferrin–selenium-G supplement (Gibco), 1 mM sodium pyruvate, 100 µg/ml heparin, 2 mM L-glutamine, 1× MEM with nonessential amino acids, 55 µM β-mercaptoethanol, 100 U/ml penicillin G, and 0.1 mg/ml streptomycin sulfate. Cells were used at passage 1 or 2 in all experiments. LMECs were isolated from neonatal pups as described previously (Fehrenbach et al., 2009). In brief, 0.5% buffered collagenase II (Worthington Biochemical

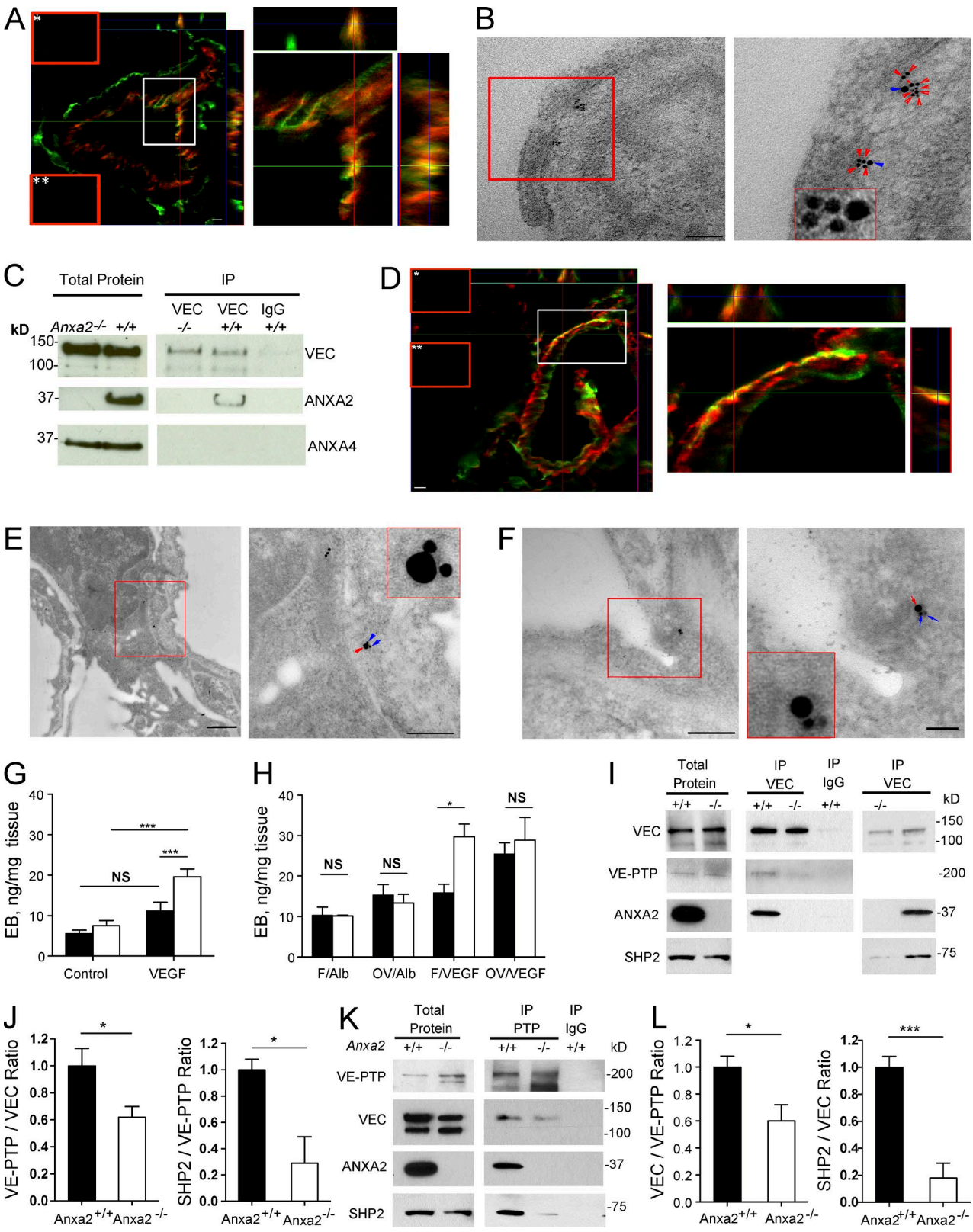

Figure 5. **ANXA2 associates with VEC, VE-PTP, and SHP2 and supports phosphatase function.** (A) Confocal image of lung section stained with FITC anti–ANXA2 IgG (green) and Cy3 anti–VEC IgG (red, left; enlarged, right). Subpanels outlined in red show no primary control–stained section for anti-ANXA2 (*) and anti-VEC (**). Bar, 10 µm. (B) IEM image of pulmonary microvessel stained with anti-ANXA2 and anti-VEC (10-nm and 6-nm gold conjugates, blue

Corporation) was instilled into the lungs through the trachea. After 45 min of tissue dissociation, cells were collected and ECs purified using anti–CD31-conjugated magnetic microbeads (MACS, #130-097-418).

For assessment of permeability, CMECs or LMECs were seeded on fibronectin-coated, 0.4-µm pore, polyester Transwell inserts (1×10^5 cells/well; Corning) positioned in 12-well cluster dishes. Culture medium was replaced with phenol red-free, serum-free DMEM on day 2 of confluency (Su et al., 2010). FITC–dextran (500 kD, 100 µg; D7136; Invitrogen; or 2,000 kD, 250 µg; D7137; Invitrogen) or Texas red–dextran (40 kD, 100 µg; D1829; Invitrogen) was added to the upper chamber 16 h later (total volume 500 µl), and six separate 100-µl samples were collected from the lower chamber over the next 24 h and replaced with fresh medium to maintain a volume of 1 ml. The FITC signal was read at 494 nm and 521 nm and Texas red at 590 nm and 620 nm excitation and emission, respectively (SpectraMax Gemini; Molecular Devices). For assessment of TEER, ECs were prepared and seeded as described for assessment of permeability to FITC-dextran and TEER calculated daily (EVOM voltohmmeter; World Precision Instruments; 6–12 samples/time point; Su et al., 2010) as total resistance minus the resistance of empty inserts (Ω per square centimeter).

For viral transduction, a replication-deficient adenovirus containing a CMV-driven ANXA2 expression cassette and GFP reporter was constructed using the pAdEasy system (Huang et al., 2011). First-passage *Anxa2*$^{+/+}$ and *Anxa2*$^{-/-}$ ECs (100,000) were propagated on Transwell inserts (12-well, 0.4-µm pore) for 4 d and then infected at confluency in serum-free medium with empty or ANXA2-encoding adenoviruses (1,000 particles per cell; efficiency of infection 60% by fluorescence microscopy; after 4 h, the medium was replaced with regular medium). At 48 h, any remaining virus was removed by washing and TEER and FITC–dextran permeability measured.

Experimental animals

All animal studies were approved by the Institutional Animal Care and Use Committee. 10–14-wk-old *Anxa2*$^{-/-}$ mice on the C57BL/6 background were generated as described previously (Ling et al., 2004). Control wild-type mice were bred on the same background in parallel to ANXA2-deficient mice. To generate *S100a10*$^{-/-}$ mice, a pPNT-based targeting vector was constructed using the neomycin resistance (Neo^R) and thymidine kinase genes as positive and negative selectors, respectively. A 5.8-kb *Not* I genomic fragment containing the mouse *S100A10* promoter, exon 1 and intron 1 was introduced into a *Not* I site upstream of Neo^R cassette within the pPNT vector. A second 1.5-kb BamHI fragment including part of exon 3 and all of the 3′ UTR was subcloned into the BamHI site downstream of the Neo^R gene but upstream of the thymidine kinase gene of the pPNT vector. In addition, a 1-kb EGFP sequence was cloned into pPNT between the NotI site and the Neo^R cassette. Finally, the 5.8-kb long arm and 1.5-kb short arm flanking the EGFP and neomycin-resistance gene were created from *S100A10* sequences, whereas the *tk* gene remained outside of the regions of S100A10 homology.

The *S100a10* targeting vector, pPNT-S100A10, was linearized with PacI and electroporated (400 V, 25 µF; Bio-Rad) into E14-1-1 embryonic stem cells derived from 129/Ola mice. Embryonic stem cell clones selected by 400 µg/ml G418 (Gibco) and ganciclovir (2 µM; Roche) were screened by Southern blot hybridization. Two embryonic stem cell clones containing the disrupted *S100a10* allele were introduced into blastocysts of C57BL/6 embryos and injected into the uteri of pseudopregnant foster mothers. Chimeric males were identified based on agouti coat color, and then mated with C57BL/6 females. Agouti offspring were genotyped by Southern hybridization, whereby SacI-digested DNA was electrophoresed on 0.7% agarose gels and blotted onto nylon membranes. A 733-bp 3′ probe, representing sequences external to the targeting vector sequence and detecting 9.4-kb and 9.7-kb fragments of wild-type and mutant alleles, respectively, was random primer labeled (Roche). Four of 300 embryonic stem cell clones showed homologous recombination of pPNT-*S100a10* with 3′ flanking probes. For PCR genotyping of DNA isolated from tail biopsies, oligonucleotide primers included 5′-TCAGCACTTACTTCCAAAAACCC-3′ (reverse), which is specific for wild-type, 5′-AGCTTGCCG GTGGTGCAGATGAACTTC-3′ (reverse), which is specific

and red arrows, respectively, left; enlarged, right). Bars: (left) 100 nm; (right) 50 nm. (C) Lung tissue extracts immunoprecipitated (IP) with anti–VEC or nonimmune IgG and immunoblotted for VEC, ANXA2, and ANXA4. (D) Confocal image of lung section stained with stained with FITC anti–ANXA2 IgG (green) and Cy3 anti–VE-PTP IgG (red, left; enlarged, right). Subpanels outlined in red show no primary control–stained section for anti-ANXA2 (*) and anti-VE-PTP (**). Bar, 10 µm. (E) IEM images of pulmonary microvessel stained with anti-PTP and anti-ANXA2 (10-nm and 6-nm gold conjugates, red and blue arrows, respectively, left; enlarged, right). Bars: (left) 500 nm; (right) 200 nm. (F) Pulmonary microvessel stained with anti-PTP and anti-VEC followed by gold-conjugated (10- and 6-nm conjugates, red and blue arrows, respectively, left; enlarged, right). Bars: (left) 200 nm; (right) are 50 nm. (G) Miles assay (conducted as described in Materials and methods) to assess VEGF-induced cutaneous EB extravasation in *Anxa2*$^{+/+}$ and *Anxa2*$^{-/-}$ mice (n = 7–8 mice per group, ANOVA). (H) Effect of Na_3VO_4 (sodium orthovanadate [OV]) or 100 µl, 5 mM sodium fluoride (NaF; subcutaneously, n = 8 mice per group, ANOVA) on VEGF-induced cutaneous EB extravasation. (I) Extracts of lung tissue immunoprecipitated with anti-VEC and immunoblotted for VEC, VE-PTP, SHP2, and ANXA2. (J) Quantification of immunoprecipitated bands in I (data combined from four experiments, Student's t test). (K) Extracts of lung tissue were immunoprecipitated with anti–VE-PTP and immunoblotted for VE-PTP, VEC, ANXA2, and SHP2. (L) Quantification of immunoprecipitated bands in K (data combined from four experiments, Student's t test). Data in A–I and in J–L are representative of three and four experiments, respectively. Black and white bars indicate *Anxa2*$^{+/+}$ and *Anxa2*$^{-/-}$ mice, respectively. Data are expressed as mean ± SEM. *, $P < 0.05$; ***, $P < 0.001$.

for the targeted allele, and 5′-CTCTCTTTATGTCCTTTA ACAGGTTTCGACAGACTCTTC-3′ (forward), which is common to both genotypes. Heterozygous mice were crossbred with C57BL/6 mice at least seven times, and the resultant heterozygotes were interbred to obtain the wild-type and knockout mice used in the present study.

O_2 deprivation and capillary integrity

Mice were maintained for 48 h in a normobaric BioSpherix A chamber equipped with an E702 O_2 sensor and a ProOx P110 O_2 controller preset to deliver 10 ± 0.4% O_2 by using room air/N_2 at a ratio of 10:11 (Costello et al., 2008). Hemoglobin O_2 saturation was assessed as 10 stable readings via the left anterior paw using a MouseSTAT pulse oximeter (Kent Scientific) and paw sensor (MSTAT sensor-MSE; Pilling et al., 2007) within 10 min of returning to room air. VEGF in citrated platelet-poor plasma, prepared by two rounds of centrifugation (300 *g*, 15 min, 21°C), was measured by ELI SA (MMV00; R&D Systems).

Weights of nonperfused brain, liver, heart and lung, excised *en bloc* and freed of extraneous tissue, were recorded before and after placement in a desiccating oven (65°C, 48 h) to calculate wet/dry ratios. For BAL, lungs of deeply anesthetized mice were lavaged three times via tracheotomy with 0.5 ml PBS containing 0.9 mM $CaCl_2$ and 0.5 mM $MgCl_2$. Retrieved BAL fluid was pooled and adjusted the final volume to 1 ml. Albumin levels were determined by ELISA (1000-1; Life Diagnostics) in centrifuged (1,000 *g*, 5 min, 4°C) BAL fluid diluted 1:3,000 (Eckle et al., 2013).

For assessment of capillary integrity, *Anxa2*$^{+/+}$ and *Anxa2*$^{-/-}$ mice received a single tail vein injection of 60 mg/kg EB (Sigma-Aldrich) in 100 µl normal saline immediately upon release from hypoxia. 3 h later, lungs were removed from extensively perfused mice, homogenized, extracted in 2 vol formamide (18 h, 60°C), and centrifuged (5,000 *g*, 30 min). Optical density of the supernatant was determined spectrophotometrically at 620 nm (Yepes et al., 2003).

For assessment of cutaneous vascular permeability, Miles assays were conducted whereby EB was injected by tail vein (30 mg/kg in 100 µl PBS, i.v.), followed 10 min later by injection of albumin or recombinant human VEGF165 (rhVEGF165; R&D Systems; 293-VE; 50 ng in 50 µl PBS intradermally) into the shaved back (Kim et al., 2012). The animals were sacrificed 20 min later, and a standard, 1-cm^2 section of skin surrounding the injection site excised for dye extraction. In some experiments, mice received twice-daily injections of the defibrinogenating agent Ancrod (74/581; National Institute of Biological Standards and Control; 2 U in 200 µl saline) for 4 d before skin harvest. Some mice were pretreated subcutaneously with either 5 mM of the phosphatase inhibitor sodium orthovanadate (P0758; New England Biolabs) or 5 mM of the control inhibitor sodium fluoride (P0759; New England Biolabs), which inhibits protein phosphoseryl and phosphothreonyl phosphatases, but not tyrosine phosphatases. 30 min later, the mice received i.v. EB, and then either albumin or rVEGF (intradermally) after an additional 20 min. The skin was harvested 60 min later and extravasated EB quantified.

Immunoprecipitation and immunoblotting

For immunoprecipitation, extensively perfused lungs were homogenized in lysis buffer (25 mM Tris-HCl, pH 8.0, 1% Triton X-100, 150 mM NaCl, 1 mM EDTA, 1 mM PMSF, and Roche complete mini protease inhibitor), centrifuged at 15,000 *g*, and the supernatant incubated with control agarose resin (1.5 h, 4°C, with rotation). 750 µg of precleared protein extract (1 µg/µl) was incubated for 18 h with 7.5 µg mouse nonimmune versus monoclonal anti–human VEC IgG (sc-2025; Santa Cruz Biotechnology, Inc.; ab7047; Abcam; respectively), or 7.5 µg rabbit nonimmune or polyclonal anti–human VE-PTP IgG (sc-2027 and sc-28905, respectively; Santa Cruz Biotechnology, Inc.) coupled to AminoLink Plus Resin (Thermo Fisher Scientific). Immunocomplexes were immunoblotted with anti-VEC (NBP1-43347; Novus Biologicals), anti-ANXA2 (610069; BD), anti–VE-PTP (sc-28905; Santa Cruz Biotechnology, Inc.), anti-ANXA4 (NBP1-90151; Novus Biologicals), anti-SHP2 (610621; BD), and anti–β catenin (AF1329; R&D Systems).

For immunoblotting of extravascular lung albumin, total protein from highly perfused upper left lobes was extracted, resolved by SDS-PAGE, and blotted with antialbumin (ab19196; Abcam), anti-ANXA2 (BD), anti-S100A10 (AF2377; R&D Systems), anti-Ly6G (127601; BioLegend), anti-F4/80 (MCA497G; AbD Serotec), and anti-GAPDH (H86504; Biodesign). Band density was quantified using Image J software (version 3.1.4). For immunoblot analysis of VEC tyrosine phosphorylation, *Anxa2*$^{+/+}$ and *Anxa2*$^{-/-}$ ECs (300,000 per sample, P1–P4) were cultured to confluency on fibronectin-coated wells. After 16 h of serum withdrawal, the cells were treated with 50 ng/ml recombinant mouse VEGF164 (0–2 h; 493-MV; R&D Systems). Total protein was extracted with lysis buffer containing 2 mM $CaCl_2$, 1 mM Na_3VO_4, and 1× phosphatase inhibitor (1862495; Thermo Fisher Scientific) and immunoblotted with anti–pY731-VEC (441145G; Invitrogen; or rat anti-mouse pY731-VEC monoclonal [pY731-73.1], a gift from D. Vestweber; Wessel et al., 2014). In addition, cell extracts were immunoblotted with rat monoclonal hybridoma supernatant directed against mouse pY685-VEC (PhoCad3.3), a gift from D. Vestweber (Wessel et al., 2014). In some experiments, extracts were also immunoblotted with anti–pY416-Src (2101S; Cell Signaling Technology) and anti-Src (ab7950; Abcam) after treatment with 50 ng/ml rmVEGF, 1 µM of the Src kinase inhibitor PP2 (529573; EMD Millipore), or 1 µM of the PP3 control (529574; EMD Millipore) before immunoblotting or permeability testing.

Histology and immunohistochemistry

5-µm, 4% paraformaldehyde–fixed, paraffin-embedded sections from extensively perfused lung tissue were subjected

to both hematoxylin and eosin staining. Twenty fields of hematoxylin and eosin–stained lung sections from each of three highly perfused *Anxa2*$^{+/+}$ or *Anxa2*$^{-/-}$ mice maintained at FiO_2 of either 0.21 or 0.10 for 48 h were scored and averaged using a standard mouse lung injury system (Aeffner et al., 2015).

For immunostaining, paraffin-embedded, 4% paraformaldehyde–fixed (18 h, 4°C) sections were deparaffinized in Histoclear (National Diagnostics) and rehydrated in a graded ethanol series. Antigen retrieval was performed by steam heating slides in 0.01 M sodium citrate (pH 6, 0.05% Tween 20; 2100 Antigen Retriever; Pick Cell Laboratories). To reduce autofluorescence, all sections were preincubated with sodium borohydride (1%, 5 min) immediately before blocking. For extravascular albumin staining, sections were incubated with rabbit anti-albumin IgG (Abcam) followed by Cy3-conjugated donkey anti-rabbit IgG. Staining was quantified using NIS-Elements BR3.1 software. For VEC and ANXA2 coimmunostaining, sections were stained (18 h, 4°C) with goat anti-VEC (AF1002; R&D Systems) and rabbit anti–ANXA2 IgG (sc-9061; Santa Cruz Biotechnology, Inc.), followed by FITC-conjugated donkey anti–rabbit and Cy3-conjugated donkey anti–goat IgG, respectively. For ANXA2 and VE-PTP coimmunostaining, antigen-retrieved sections were blocked with mouse IgG and then incubated with mouse anti–ANXA2 IgG (610069; BD; 18 h, 4°C), followed by Alexa 488–conjugated donkey anti–mouse IgG. Subsequently, the same sections were labeled with rabbit anti–VE-PTP IgG (sc28905; Santa Cruz Biotechnology, Inc.; 2 h, 37°C), followed by Cy3-conjugated donkey anti–rabbit IgG.

For IEM imaging, highly perfused lung tissue was fixed with 4% paraformaldehyde/0.1% glutaraldehyde, dehydrated, and embedded in Lowicryl HM20. Unreacted aldehydes were quenched with 50 mM glycine in PBS, and blocked, ultrathin (100-nm) sections were incubated with a goat anti–VEC IgG (AF1002; R&D Systems) and rabbit anti–ANXA2 IgG (sc-9061; Santa Cruz Biotechnology, Inc.) mixture, rabbit anti–VE-PTP IgG (sc28905; Santa Cruz Biotechnology, Inc.) and goat anti–ANXA2 IgG (sc-30757; Santa Cruz Biotechnology, Inc.), or rabbit anti–VE-PTP IgG and goat anti–VEC IgG. Incubations were followed by labeling with 10-nm anti–rabbit and 6-nm anti–goat IgG–conjugated gold particles (Aurion). Images were captured on a Veleta CCD camera (SIS; Olympus) mounted on a JEOL 1400 electron microscope. Single and no primary antibody controls were performed in parallel in both genotypes.

Statistical analyses

Student's *t* test was used to compare the means of data from two experimental groups. One-way ANOVA was used when three or more experimental groups were compared, and analysis of significance was performed using Tukey's range test (*, $P < 0.05$; **, $P < 0.01$; ***, $P < 0.001$). Data are expressed as mean ± SEM.

ACKNOWLEDGMENTS

We thank Christopher Huber and Dr. Arun Deora for technical assistance and advice and Prof. Dietmar Vestweber for the gift of phospho-VEC–specific antibodies. IEM was performed in the Weill Cornell Imaging Core Facility with assistance from Lee Cohen-Gould.

This work was supported by National Institutes of Health grants HL042493 and MOD #6-FY15-226 (to K.A. Hajjar).

The authors declare no competing financial interests.

Submitted: 5 May 2016
Revised: 14 March 2017
Accepted: 31 May 2017

REFERENCES

Aeffner, F., B. Bolon, and I.C. Davis. 2015. Mouse models of acute respiratory distress syndrome: A review of analytical approaches, pathologic features, and common measurements. *Toxicol. Pathol.* 43:1074–1092. http://dx.doi.org/10.1177/0192623315598399

Burkart, A., B. Samii, S. Corvera, and H.S. Shpetner. 2003. Regulation of the SHP-2 tyrosine phosphatase by a novel cholesterol- and cell confluence-dependent mechanism. *J. Biol. Chem.* 278:18360–18367. http://dx.doi.org/10.1074/jbc.M210701200

Costello, C.M., K. Howell, E. Cahill, J. McBryan, M. Konigshoff, O. Eickelberg, S. Gaine, F. Martin, and P. McLoughlin. 2008. Lung-selective gene responses to alveolar hypoxia: Potential role for the bone morphogenetic antagonist gremlin in pulmonary hypertension. *Am. J. Physiol. Lung Cell. Mol. Physiol.* 295:L272–L284. http://dx.doi.org/10.1152/ajplung.00358.2007

Dejana, E., and D. Vestweber. 2013. The role of VE-cadherin in vascular morphogenesis and permeability control. *Prog. Mol. Biol. Transl. Sci.* 116:119–144. http://dx.doi.org/10.1016/B978-0-12-394311-8.00006-6

Durr, E., J.Yu, K.M. Krasinska, L.A. Carver, J.R.Yates, J.E.Testa, P. Oh, and J.E. Schnitzer. 2004. Direct proteomic mapping of the lung microvascular endothelial cell surface in vivo and in cell culture. *Nat. Biotechnol.* 22:985–992. http://dx.doi.org/10.1038/nbt993

Eckle, T., K. Hughes, H. Ehrentraut, K.S. Brodsky, P. Rosenberger, D.S. Choi, K. Ravid, T. Weng, Y. Xia, M.R. Blackburn, and H.K. Eltzschig. 2013. Crosstalk between the equilibrative nucleoside transporter ENT2 and alveolar Adora2b adenosine receptors dampens acute lung injury. *FAS EB J.* 27:3078–3089. http://dx.doi.org/10.1096/fj.13-228551

Fehrenbach, M.L., G. Cao, J.T. Williams, J.M. Finklestein, and H.M. Delisser. 2009. Isolation of murine lung endothelial cells. *Am. J. Physiol. Lung Cell. Mol. Physiol.* 296:L1096–L1103. http://dx.doi.org/10.1152/ajplung.90613.2008

Grinnell, K.L., B. Casserly, and E.O. Harrington. 2010. Role of protein tyrosine phosphatase SHP2 in barrier function of pulmonary endothelium. *Am. J. Physiol. Lung Cell. Mol. Physiol.* 298:L361–L370. http://dx.doi.org/10.1152/ajplung.00374.2009

Heemskerk, N., M. Asimuddin, C. Oort, J. van Rijssel, and J.D. van Buul. 2016. Annexin A2 limits neutrophil transendothelial migration by organizing the spatial distribution of ICAM-1. *J. Immunol.* 196:2767–2778. http://dx.doi.org/10.4049/jimmunol.1501322

Heyraud, S., M. Jaquinod, C. Durmort, E. Dambroise, E. Concord, J.P. Schaal, P. Huber, and D. Gulino-Debrac. 2008. Contribution of annexin 2 to the architecture of mature endothelial adherens junctions. *Mol. Cell. Biol.* 28:1657–1668. http://dx.doi.org/10.1128/MCB.00695-07

Huang, B., A.B. Deora, K.L. He, K. Chen, G. Sui, A.T. Jacovina, D. Almeida, P. Hong, P. Burgman, and K.A. Hajjar. 2011. Hypoxia-inducible factor-1 drives annexin A2 system-mediated perivascular fibrin clearance in oxygen-induced retinopathy in mice. *Blood*. 118:2918–2929. http://dx.doi.org/10.1182/blood-2011-03-341214

Kaner, R.J., J.V. Ladetto, R. Singh, N. Fukuda, M.A. Matthay, and R.G. Crystal. 2000. Lung overexpression of the vascular endothelial growth factor gene induces pulmonary edema. *Am. J. Respir. Cell Mol. Biol.* 22:657–664. http://dx.doi.org/10.1165/ajrcmb.22.6.3779

Kim, S.H., Y.R. Cho, H.J. Kim, J.S. Oh, E.K. Ahn, H.J. Ko, B.J. Hwang, S.J. Lee, Y. Cho, Y.K. Kim, et al. 2012. Antagonism of VEGF-A-induced increase in vascular permeability by an integrin α3β1-Shp-1-cAMP/PKA pathway. *Blood*. 120:4892–4902. http://dx.doi.org/10.1182/blood-2012-05-428243

Küppers, V., M. Vockel, A.F. Nottebaum, and D. Vestweber. 2014. Phosphatases and kinases as regulators of the endothelial barrier function. *Cell Tissue Res.* 355:577–586. http://dx.doi.org/10.1007/s00441-014-1812-1

Ling, Q., A.T. Jacovina, A. Deora, M. Febbraio, R. Simantov, R.L. Silverstein, B. Hempstead, W.H. Mark, and K.A. Hajjar. 2004. Annexin II regulates fibrin homeostasis and neoangiogenesis in vivo. *J. Clin. Invest.* 113:38–48. http://dx.doi.org/10.1172/JCI19684

Luo, M., and K.A. Hajjar. 2013. Annexin A2 system in human biology: Cell surface and beyond. *Semin. Thromb. Hemost.* 39:338–346. http://dx.doi.org/10.1055/s-0033-1334143

Manalo, D.J., A. Rowan, T. Lavoie, L. Natarajan, B.D. Kelly, S.Q. Ye, J.G.N. Garcia, and G.L. Semenza. 2005. Transcriptional regulation of vascular endothelial cell responses to hypoxia by HIF-1. *Blood*. 105:659–669. http://dx.doi.org/10.1182/blood-2004-07-2958

Nawroth, R., G. Poell, A. Ranft, S. Kloep, U. Samulowitz, G. Fachinger, M. Golding, D.T. Shima, U. Deutsch, and D. Vestweber. 2002. VE-PTP and VE-cadherin ectodomains interact to facilitate regulation of phosphorylation and cell contacts. *EMBO J.* 21:4885–4895. http://dx.doi.org/10.1093/emboj/cdf497

Nottebaum, A.F., G. Cagna, M. Winderlich, A.C. Gamp, R. Linnepe, C. Polaschegg, K. Filippova, R. Lyck, B. Engelhardt, O. Kamenyeva, et al. 2008. VE-PTP maintains the endothelial barrier via plakoglobin and becomes dissociated from VE-cadherin by leukocytes and by VEGF. *J. Exp. Med.* 205:2929–2945. http://dx.doi.org/10.1084/jem.20080406

Orsenigo, F., C. Giampietro, A. Ferrari, M. Corada, A. Galaup, S. Sigismund, G. Ristagno, L. Maddaluno, G.Y. Koh, D. Franco, et al. 2012. Phosphorylation of VE-cadherin is modulated by haemodynamic forces and contributes to the regulation of vascular permeability in vivo. *Nat. Commun.* 3:1208–1223. http://dx.doi.org/10.1038/ncomms2199

Pilling, D., D. Roife, M. Wang, S.D. Ronkainen, J.R. Crawford, E.L. Travis, and R.H. Gomer. 2007. Reduction of bleomycin-induced pulmonary fibrosis by serum amyloid P. *J. Immunol.* 179:4035–4044. http://dx.doi.org/10.4049/jimmunol.179.6.4035

Su, S.C., S.A. Maxwell, and K.J. Bayless. 2010. Annexin 2 regulates endothelial morphogenesis by controlling AKT activation and junctional integrity. *J. Biol. Chem.* 285:40624–40634. http://dx.doi.org/10.1074/jbc.M110.157271

Townsley, M.I. 2012. Structure and composition of pulmonary arteries, capillaries, and veins. *Compr. Physiol.* 2:675–709. http://dx.doi.org/10.1002/cphy.c100081

Vockel, M., and D. Vestweber. 2013. How T cells trigger the dissociation of the endothelial receptor phosphatase VE-PTP from VE-cadherin. *Blood*. 122:2512–2522. http://dx.doi.org/10.1182/blood-2013-04-499228

Wessel, F., M. Winderlich, M. Holm, M. Frye, R. Rivera-Galdos, M. Vockel, R. Linnepe, U. Ipe, A. Stadtmann, A. Zarbock, et al. 2014. Leukocyte extravasation and vascular permeability are each controlled in vivo by different tyrosine residues of VE-cadherin. *Nat. Immunol.* 15:223–230. http://dx.doi.org/10.1038/ni.2824

Yepes, M., M. Sandkvist, E.G. Moore, T.H. Bugge, D.K. Strickland, and D.A. Lawrence. 2003. Tissue-type plasminogen activator induces opening of the blood-brain barrier via the LDL receptor-related protein. *J. Clin. Invest.* 112:1533–1540. http://dx.doi.org/10.1172/JCI200319212